Wave Excitation Force Estimation for a Multi-DoF WEC via a Cubature Kalman Filter: Improved Design and Results

Jiamin Zhu, Alexis Mérigaud, and Paolino Tona

Abstract—**In this study, we propose a nonlinear multi-degree-of-freedom wave excitation force estimator for a CETO-like device, a submerged wave energy converter powered by three power take-off systems. Our approach combines the square-root cubature Kalman filter (SCKF), with a heuristic covariance adaptation method. This method is developed based on a numerical sensitivity analysis and is shown to be easily implementable and extendable. Only 3 hyper-parameters need to be tuned offline for a single sea state, and the resulting tuning achieves quite good estimation performance across a wide range of sea states.**

Index Terms—**Wave energy converters, wave excitation force estimation, Kalman filters, error covariance matrix adaptation heuristic.**

I. INTRODUCTION

MANY advanced control methods for power maximisation of wave energy converters (WECs) require online estimation of wave excitation forces. While most published studies address the estimation problem for WECs with one degree of freedom (DoF), the existing literature is relatively scarce for multi-DoF devices. Reference [1], which explores wave excitation force estimation and prediction for a spar-buoy WEC, is likely the earliest published study addressing the 3-DoF context. It introduces an extended Kalman filter approach that treats the wave excitation force as a combination of time-varying sinusoids. On average, simulation results demonstrate accurate estimation in the heave direction, but less satisfactory performance in the surge and pitch directions, with a significant deterioration for some of the considered sea states. In [2], a multi-DOF extension of the "simple-but-effective" controller is developed for a WaveSub-like device, a 4-PTO submerged WEC, while in [3] a model predictive control (MPC) approach is introduced for the same device. While the estimation results presented in [2] for the surge and heave directions appear perfect, no details regarding the dynamic observer are provided. Conversely, in [3], the authors mention utilizing a 3-DoF extension of the Kalman Filter approach proposed in [4]. In the latter study, the plots indicate appreciable discrepancy between the estimated wave and the "true" excitation force in the surge and heave directions. However, no results are provided for the pitch direction, nor for off-axis loading scenarios that would induce excitation in other directions.

Undoubtedly, the design of a multi-DoF excitation force estimator presents various challenges. Indeed, the high dimension of the underlying dynamic system poses difficulties in both online implementation and estimator parameter-tuning. In addition, multi-DoF systems are associated with specific non-linear effects, stemming from the kinematic terms. Those effects may lead to a substantial performance deterioration, if the estimator relies on a linearized model to reduce computation time. Therefore, an efficient nonlinear estimator is desirable.

Among the various Kalman-like nonlinear filters, the extended Kalman filter (EKF) and the unscented Kalman filter (UKF) have emerged as the most commonly utilized approaches for estimator design. In both EKF and UKF, the state distribution is approximated by a Gaussian random variable. While in the EKF this distribution is propagated analytically through the (first-order) linearization of the nonlinear system, in the UKF, this distribution is approximated using a set of carefully chosen sample points (called sigma points) and is propagated through the true nonlinear system [5]. In [6], it has been pointed out that the simpler form of the UKF obtained by setting the nonzero scaling parameter (defining the nonzero center sigma point), corresponds to the Cubature Kalman Filter (CKF), which is derived directly from the cubature integration rules. The advantage of the CKF is that it does not have any free parameter to be tuned, if the process and the observation error covariances are known. The CKF appears to be numerically accurate and can be easily extended to high-dimensional problems. However, several operations in the CKF algorithm, such as matrix square-rooting and matrix inversion, can destroy the symmetry and the (semi-)positive definiteness of covariance matrices. Some nonlinear filtering problems can also be numerically ill-conditioned. A remedy to this problem is the square-root extension of the CKF, known as SCKF (square-root cubature Kalman filter), which preserves the desired properties of covariance matrices and increases numerical accuracy.

As for the wave excitation force estimation problem,

Jiamin Zhu and Alexis Mérigaud are with IFP Energies nouvelles, 1-4 Avenue du Bois Préau, 92852 Rueil-Malmaison, France. (e-mails: jiamin.zhu@ifpen.fr, alexis.merigaud@ifpen.fr)

Paolino Tona is with IFP Energies nouvelles, Lyon Rond-point de l'échangeur de Solaize, BP 369360 Solaize, France. (e-mail: paolino.tona@ifpen.fr)

Digital Object Identifier:
https://doi.org/10.36688/ewtec-2023-468

a CKF wave excitation force estimator was proposed in [7], based on a linear state-space model. Regrettably, undesirable large estimation errors on yaw were observed for several scenarios, primarily attributed to model errors resulting from kinematics linearization. Furthermore, although the CKF (and SCKF) are known to be straightforward to apply, the tuning of covariance matrices of the process and observation model noises remains troublesome.

In this paper, to jointly address the challenges of parameter tuning and nonlinear estimation accuracy, we propose the more robust SCKF, in conjunction with a heuristic method to adjust the error covariance matrix. In our estimator, a nonlinear dynamic system of dimension 72 is used to predict the system dynamics at the cubature points, and to estimate the 6-dimensional excitation force. In addition, we show that careful scaling of system state can substantially reduce estimation errors on yaw. Furthermore, thanks to the parallelization capability and moderate computational complexity of the SCKF, online implementation becomes feasible by slightly increasing the sampling time step, albeit at the price of a minor performance degradation.

It is important to highlight that our heuristic covariance adaptation method, despite being founded on a numerical sensitivity analysis and requiring calibration of several hyper-parameters, holds practical significance. This is because it is easy to calibrate and seems to be easily extendable to other estimation problems. For our wave force estimator, according to the sensitivity analysis, only 3 hyper-parameters are to be tuned. Numerical results show that, these hyper-parameters do not need to be tuned based on simulations performed on a wide range of expected sea conditions: we only need to tune and fix them with respect to a single sea state.

This paper is organized as follows. In section (II), we recall the SCKF algorithm and present a brief stability analysis, with respect to the covariance matrices tuning parameters. In section III, we show how the SCKF is applied to our wave excitation force estimation problem. Finally, Section IV shows numerical results, and conclusions are drawn in Section V.

II. SQUARE ROOT CUBATURE KALMAN FILTER

Assuming Gaussian conditional densities, the key to Bayesian filters is the computation of Gaussian weighted integrals, the integrands of which are the product of a nonlinear function with a Gaussian density. The main idea of the CKF is to approximate these integrals using the cubature integration rules, which are known to be numerically efficient. Compared to the CKF, the SRCKF introduces two additional techniques to improve numerical stability: the least-squares method for the Kalman gain and the matrix triangular factorizations or triangularizations for the covariance updates.

Consider the following process and observation models

$$x_k = f(x_{k-1}, u_{k-1}) + v_{k-1} \tag{1}$$

$$z_k = h(x_k) + w_k \tag{2}$$

where $x_k \in \mathbf{R}^{n_x}$ and $z_k \in \mathbf{R}^{n_z}$ represent the system state and measurement at time k, $f : \mathbf{R}^{n_x} \mapsto \mathbf{R}^{n_x}$ and $h : \mathbf{R}^{n_x} \mapsto \mathbf{R}^{n_z}$ are some known functions, $\{v_k\}$ and $\{w_k\}$ are independent process and measurement Gaussian noise sequences with zero means and covariances Q_k and R_k, respectively.

A. SCKF algorithm

In the following, $Tria(\cdot)$ denotes a general triangularization algorithm (e.g., the QR decomposition) resulting in a lower triangular matrix. We summarize the square-root cubature Kalman filter (SCKF) algorithm as below.

Setup. Let $m = 2n_x$, and generate the cubature points

$$\xi_i = \begin{cases} \sqrt{n_x}\mathbf{e}_i, & i = 1, \cdots, n_x \\ \sqrt{n_x}\mathbf{e}_{i-n_x}, & i = n_x + 1, \cdots, 2n_x \end{cases}$$

where $\mathbf{e}_i$ denotes the ith-column vector of the identity matrix I_{n_x}.

Time Update

1) Evaluate the cubature points for $i = 1, \cdots, m$

$$\mathbf{X}_{i,k-1|k-1} = S_{k-1|k-1}\xi_i + \hat{x}_{k-1|k-1}. \tag{3}$$

2) Evaluate the propagated cubature points for $i = 1, \cdots, m = 2n_x$

$$\mathbf{X}^*_{i,k|k-1} = f(\mathbf{X}_{i,k-1|k-1}, u_{k-1}). \tag{4}$$

3) Estimate the predicted state

$$\hat{x}_{k|k-1} = \frac{1}{m}\sum_{i=1}^{m} \mathbf{X}^*_{i,k|k-1}. \tag{5}$$

4) Estimate the square-root factor of the predicted error covariance

$$S_{k|k-1} = Tria\left(\left[\mathcal{X}^*_{k|k-1} \quad S_{Q,k-1}\right]\right), \tag{6}$$

where $S_{Q,k-1}$ denotes a square-root factor of Q_{k-1} such that $Q_{k-1} = S_{Q,k-1}S^T_{Q,k-1}$ and the weighted, centered (prior mean is substracted off) matrix

$$\mathcal{X}^*_{k|k-1} = \frac{1}{\sqrt{m}}[\mathbf{X}^*_{1,k|k-1} - \hat{x}_{k|k-1}, \cdots, \mathbf{X}^*_{m,k|k-1} - \hat{x}_{k|k-1}].$$

Measurement Update

1) Evaluate the cubature points for $i = 1, \cdots, m$

$$\mathbf{X}_{i,k|k-1} = S_{k|k-1}\xi_i + \hat{x}_{k|k-1}. \tag{7}$$

2) Evaluate the propagated cubature points $i = 1, \cdots, m$

$$\mathbf{Z}_{i,k|k-1} = h(X_{i,k|k-1}). \tag{8}$$

3) Estimate the predicted measurement

$$\hat{z}_{k|k-1} = \frac{1}{m}\mathbf{Z}_{i,k|k-1}.$$

4) Estimate the cross-covariance matrix

$$P_{xz,k|k-1} = \mathcal{X}_{k|k-1}\mathcal{Z}^T_{k|k-1}, \tag{9}$$

with the weighted, centered matrices

$$\mathcal{X}_{k|k-1} = \frac{1}{\sqrt{m}}[\mathbf{X}_{1,k|k-1} - \hat{x}_{k|k-1}, \cdots, \mathbf{X}_{m,k|k-1} - \hat{x}_{k|k-1}],$$

$$\mathcal{Z}_{k|k-1} = \frac{1}{\sqrt{m}}[\mathbf{Z}_{1,k|k-1} - \hat{z}_{k|k-1}, \cdots, \mathbf{Z}_{m,k|k-1} - \hat{z}_{k|k-1}].$$

5) Compute the matrices T_{11}, T_{21}, T_{22} using a triangularization algorithm

$$\begin{pmatrix} T_{11} & \mathbf{O} \\ T_{21} & T_{22} \end{pmatrix} = Tria \begin{pmatrix} \mathcal{Z}_{k|k-1} & S_{R,k} \\ \mathcal{X}_{k|k-1} & \mathbf{O}, \end{pmatrix} \tag{10}$$

where $S_{R,k}$ denotes a square-root factor of R_k such that $R_k = S_{R,k}S^T_{R,k}$, $T_{11} \in \mathbf{R}^{n_z \times n_z}$ and $T_{22} \in \mathbf{R}^{n_x \times n_x}$ are lower-triangular matrices, and $T_{21} \in \mathbf{R}^{n_x \times n_z}$.

6) Estimate the Kalman gain

$$W_k = T_{21}T_{11}^{-1}. \tag{11}$$

7) Estimate the updated state

$$\hat{x}_{k|k} = \hat{x}_{k|k-1} + W_k(z_k - \hat{z}_{k|k-1}). \tag{12}$$

8) Estimate the square-root factor of the corresponding error covariance

$$S_{k|k} = T_{22}.$$

For the full mathematical derivation of the SCKF , the interested reader is referred to papers [6], [8].

Remark 1: A usual choice for the matrices Q_k and R_k are the covariances for the noise terms in (1)-(2). However, these covariances are generally not known a-priori, and other options exist: in deterministic estimation problems without any noise, for instance, this particular choice is not applicable.

As a matter of fact, the choice of matrices Q_k and R_k can impact the stability and accuracy of the SCKF algorithm. In the next section, we provide a brief analysis that sheds light on how to design the matrix Q_k.

B. Stability analysis of SCKF

We restrict the stability analysis to the linear observation model case

$$z_k = Cx_k + w_k,$$

since it is the case for our WEC force application - see Section III. Let us define the estimation error

$$e_{k+1} = x_{k+1} - \hat{x}_{k+1|k+1}, \tag{13}$$

the prediction error

$$e_{k+1|k} = x_{k+1} - \hat{x}_{k+1|k}, \tag{14}$$

and the innovation

$$\Delta z_{k+1|k} = z_{k+1} - \hat{z}_{k+1|k} = Ce_{k+1|k}. \tag{15}$$

The Kalman gain defined by (11) has been derived from its definition

$$W_{k+1} = P_{xz,k+1|k}P^{-1}_{zz,k+1|k},$$

with

$$P_{xz,k+1|k} = T_{21}T^T_{11} \quad P_{zz,k+1|k} = T_{11}T^T_{11}. \tag{16}$$

(see details in [8]). In the linear measurement model case, we can rewrite the Kalman gain as

$$W_{k+1} = P_{k+1|k}C^T P^{-1}_{zz,k+1|k}.$$

Then, by definitions (13)-(14) and (12), we have

$$\begin{aligned} e_{k+1} &= e_{k+1|k} - W_{k+1}\Delta z_{k+1} \\ &= \left(I - P_{k+1|k}C^T P^{-1}_{zz,k+1|k}C\right) e_{k+1|k}. \end{aligned} \tag{17}$$

Expressing x_{k+1} and $\hat{x}_{k+1|k}$ (5) as a Taylor series about $\hat{x}_{k|k}$ yields

$$\begin{aligned} x_{k+1} =& f(\hat{x}_{k|k}, u_k) + A_k e_k + \frac{1}{2}e_k^T \nabla^2 f((\hat{x}_{k|k}, u_k)e_k \\ &+ o(||e_k||^2) + v_k \ , \end{aligned}$$

$$\begin{aligned} \hat{x}_{k+1|k} =& \frac{1}{m}\sum_{i=1}^{m} f(S_{k|k}\xi_i + \hat{x}_{k|k}, u_k) \\ =& f(\hat{x}_{k|k}, u_k) + A_k \sum_{i=1}^{m} S_{k|k}\xi_i + \\ & \frac{1}{2}\sum_{i=1}^{m} \xi_i^T S^T_{k|k} \nabla^2 f((\hat{x}_{k|k}, u_k)(S_{k|k}\xi_i) + o(||S_{k|k}\xi_i||^2) \end{aligned}$$

where $A_k = \nabla f(\hat{x}_{k|k}, u_k)$. In the linear process model case, i.e., $x_{k+1} = A_k x_k + v_k$, one has simply $e_{k+1|k} = A_k e_k + v_k$. In the nonlinear model case, in order to take the higher order terms into account, we introduce, like in [9], a time-varying diagonal matrix $\beta_k = diag(\beta_{1,k}, \cdots, \beta_{n_x,k})$ such that

$$e_{k+1|k} = \beta_k A_k e_k + v_k.$$

Therefore, defining

$$\begin{aligned} D_k &:= I - P_{k+1|k}C^T P^{-1}_{zz,k+1|k}C \ , \\ \Phi(k+1,k) &:= D_k \beta_k A_k \ , \end{aligned} \tag{18}$$

the evolution of the estimation error (17) becomes

$$e_{k+1} = \Phi(k+1,k)e_k + D_k v_k. \tag{19}$$

Define $\Phi(k', k) = \Phi(k', k'-1)\Phi(k'-1, k'-2)\cdots\Phi(k+1, k)$. By definition, the distribution of $D_k v(k)$ is normal, specified by the zero means and the second moment $Q_e(k) := \mathbf{E}[(D_k v_k)(D_k v_k)^T] = D_k Q_k D_k^T$. The initial state $e(k_0)$ is also assumed normal with mean m_0 and covariance matrix $Q_{e,0}$. The solution of this normal and linear stochastic difference equation is a normal stochastic process characterized by the mean value function $m(k) = \mathbf{E}[e_k]$ given by the difference equation

$$m_{k+1} = \Phi(k+1,k)m_k, \tag{20}$$

with the initial condition $m(k_0) = m_0$, and the covariance function $R_e(k', k) = \Phi(k', k)P_e(k)$, $k' \geq k$, where $P_e(k) := \mathbf{E}[e(t)e^T(t)]$ satisfies

$$P_e(k+1) = \Phi(k+1,k)P_e(k)\Phi^T(k+1,k) + Q_e(k), \tag{21}$$

with initial condition $P(k_0) = Q_{e,0}$. The SCKF stability analysis problem thus consists in evaluating the behavior of the system (20) and (21).

The stability analysis of the mean value function equation (20) can be done via standard analysis of time-varying linear systems, see e.g. [10]–[12]. A classical result is the following: the system (20) is asymptotically stable if and only if

1) for any k_0, there exists a bound M (which may depend on k_0) such that $\|\Phi(k, k_0)\| \leq M$;
2) $\lim_{k\to\infty} \Phi(k, k_0) = 0$.

A sufficient (but conservative) condition to ensure the stability is simply to have the bound $M \leq 1$ for all k large enough. If the inequality is strict, we can get asymptotic stability. Since we have

$$\|\Phi(k+1, k)\| \leq \|I - P_{k+1|k} C^T P_{zz,k+1|k}^{-1} C\| \|\beta_k\| \|A_k\|, \tag{22}$$

we may expect to choose suitable Q_k and R_k to make the eigenvalues of $\|I - P_{k+1|k} C^T P_{zz,k+1|k}^{-1} C\|$ small enough.

We observe that a small value for R_k leads to a small value for $P_{zz,k+1|k}$ (see (16) and (10)), and hence may lead to instability.

As for the matrix Q_k, the authors of [13], [14] proposed to select it with the heuristic

$$Q_k = \left(\rho \Delta z_{k|k-1}^T \Delta z_{k|k-1} + \delta\right) I, \tag{23}$$

where ρ and δ are chosen large and small enough respectively. The idea is that when estimation error is large (resp. small), Q_k becomes large (resp. small) enough to improve stability (resp. accuracy). This heuristic has been motivated by the following observations :

- when the estimation error (innovation) is large, the values of β_k can be big and a small constant value for Q_k may lead to instability;
- a larger value for Q_k can increase the predicted error covariance $P_{k+1|k}$ (see (6)) and thus improve stability, at a price of a decrease in estimation accuracy.

In the next section, we present how we apply the SCKF to the wave excitation force estimation problem, and propose a heuristic method to tune the matrix Q_k. It is worth noting that many previous articles in the literature propose to adapt only one of the matrices R_k and Q_k, see e.g. [13]–[15]. Indeed, a large Q_k and a small R_k (resp. a small Q_k and a large R_k) indicate that we have more (resp. less) confidence on the observations than on the model. Therefore, it is generally sufficient to adjust only one of these matrices. In this paper, we will fix the matrix R_k, thus focusing solely on the tuning of Q_k.

III. APPLICATION TO THE EXCITATION FORCE ESTIMATION

A. Description and model of WEC device

As in [7], our study considers a CETO 6-like WEC. The device involves a cylindrical buoy fully submerged below the free surface, floating several meters deep, and connected to the seabed through three identical tether lines. The buoy undergoes motion in its six hydrodynamic degrees of freedom as a result of the wave excitation force. To harness this motion, each leg of the buoy is equipped with a power take-off (PTO) system, which converts the translational motion of the tethers into electrical energy. To counteract the static Archimedes force that would otherwise cause the device to ascend to the surface, each tether line is pre-tensioned. This pre-tensioning keeps the lines under tension most of the time, so that the PTOs can effectively exploit both directions of the reciprocating motion of the tethers.

The device and its main geometrical characteristics (with their notations) are shown in Figure 1.

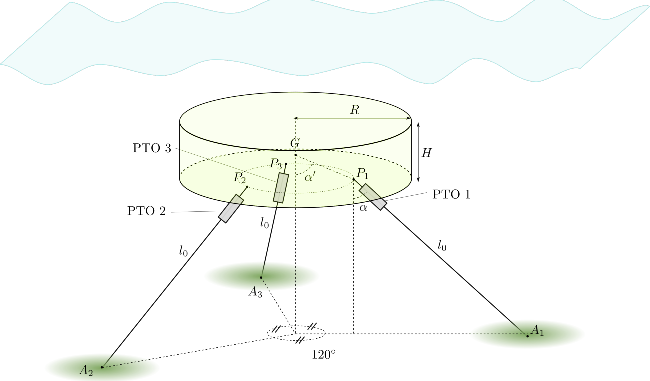

Fig. 1. The considered WEC device.

Let us denote the gravity center of the buoy as

$$\mathbf{x}_G = (x_G, y_G, z_G),$$

and the three rotations, corresponding to the Euler angles, as

$$\mathbf{\Theta} = (\theta_x, \theta_y, \theta_z).$$

There are 6 degree of freedom: surge, sway, heave, roll, pitch, yaw. Under the small motion assumption, the dynamics of the CETO system can be described by

$$M_{tot}\ddot{\mathbf{X}} = f_{rad} + f_{visc} + f_{hydstat} + f_{tether} + f_e. \tag{24}$$

where $\mathbf{X} := (\mathbf{x}_G, \mathbf{\Theta})$, $\dot{\mathbf{X}}$ and $\ddot{\mathbf{X}}$ are, respectively, the generalized position, velocity and acceleration of the buoy. M_{tot} is a diagonal matrix including the buoy mass and inertia terms for each degree of freedom. The wave excitation force f_e in the 6 degrees of freedom is considered as an unknown exogenous input of the system. The other forces are defined in the following.

Viscous forces. The viscous damping force is given by

$$f_{visc}(\dot{\mathbf{X}}) = -\mathbf{C}_v \|\dot{\mathbf{X}}\| \dot{\mathbf{X}},$$

where $\mathbf{C}_v = \frac{1}{2} C_d S_d$ is a diagonal matrix with C_d the matrix of the drag coefficients and S_d the cross-section areas of the buoy perpendicular to the direction of motion. A linearization of the viscous force leads to

$$f_{visc}(\dot{\mathbf{X}}) = B_v \dot{\mathbf{X}},$$

with B_v a constant matrix.

Hydrostatic forces. The hydrostatic force is expressed as

$$f_{hydstat}(\mathbf{X}) = -K_{hs}\mathbf{X} + f_{hs,0},$$

where K_{hs} is a matrix provided by the WAMIT hydrodynamic modelling software, and $f_{hs,0}$ is a constant vector.

Tether forces. Under the assumption of small rotation motion, the tether force f_{tether} can be given by

$$f_{tether}(\mathbf{X}, u) = \sum_{i=1}^{3} \begin{pmatrix} (T_0 + u_i)\mathbf{e}_i \\ (\mathbf{R}(\boldsymbol{\Theta})\mathbf{n}_{i0}) \times ((T_0 + u_i)\mathbf{e}_i) \end{pmatrix},$$
$$\mathbf{e}_i = \frac{\overrightarrow{A_iG_0} + \mathbf{x}_G + \mathbf{R}(\boldsymbol{\Theta})\mathbf{n}_{i0}}{\|\overrightarrow{A_iG_0} + \mathbf{x}_G + \mathbf{R}(\boldsymbol{\Theta})\mathbf{n}_{i0}\|}.$$

Here, T_0 is a pretension term, $\mathbf{R}(\boldsymbol{\Theta})$ is the rotation matrix, and $u = (u_1, u_2, u_3)$ is the vector of PTO forces exerted along each tether, i.e. the control input of the system. Note that $\mathbf{e}_i$ is the orientation of the tether i, the length of which is $l_i = \|\overrightarrow{A_iG_0} + \mathbf{x}_G + \mathbf{R}(\boldsymbol{\Theta})\mathbf{n}_{i0}\|$.

The tether force can be linearized under the assumption of small disturbances f_e and control inputs u_i. The linearized tether force can be written as

$$f_{tether}(\mathbf{X}, u) = B_u u,$$

where the matrix B_u projects control forces to the buoy centre of gravity. Note that the length l_i and the length time-derivative $\dot{l}_i$ of each tether can then be related to the buoy position and velocity through a matrix $C_{l,i}$, i.e. $l_i = l_0 + C_{l,i}\mathbf{X}$, $\dot{l}_i = C_{l,i}\dot{\mathbf{X}}$.

Radiation forces. The radiation force f_{rad} is given by

$$f_{rad}(\dot{\mathbf{X}}, \ddot{\mathbf{X}}) = -A_\infty\ddot{\mathbf{X}} - K_{rad}(t) * \dot{\mathbf{X}}(t), \tag{25}$$

where A_∞ is the added mass at infinite frequency, and $K_{rad}(t)$ is the radiation kernel response, obtained from a boundary element method (BEM) hydrodynamic database for the buoy. For control design and implementation, as well as for efficient time-domain simulations, the convolution integral term can be advantageously replaced by a state-space approximation [16]:

$$\begin{cases} \dot{\mathbf{X}}_r = A_r\mathbf{X}_r + B_r\dot{\mathbf{X}} \\ K_{rad}(t) * \dot{\mathbf{X}}(t) = C_r\mathbf{X}_r. \end{cases} \tag{26}$$

This approximation can be obtained by identifying a state-space model from BEM-computed frequency-domain data, namely the radiation kernel frequency response $\hat{K}_{rad}$:

$$\hat{K}_{rad} = B_{rad}(\omega) + j\omega(A_{rad}(\omega) - A_\infty) \tag{27}$$

Following the same approximation procedure described in [7], the resulting full state space radiation model (26) has an order of 54.

Further details on the modelling approach can be found in [17], where a similar approach is presented for a generic three-tether, fully-submersed point absorber.

B. State process and observation models

In order to apply the SCKF, we need to build process and observation models of the form (1)-(2). The main idea of the Kalman filter-based approach is to consider the wave excitation force f_e as a state. For the sake of simplicity [4], a random walk model is used to represent this additional state

$$f_e(k+1) = f_e(k) + v_e(k), \tag{28}$$

where $v_e(k)$ describes the variation of $f_e(k)$ and is considered as a random number. This model assumes that, at each sampling time, the wave excitation force takes a random step away from its previous value, and the steps are independently and identically distributed in size.

Let us define the state of the estimation system as

$$x := (\mathbf{X}, \dot{\mathbf{X}}, \mathbf{X}_r, f_e). \tag{29}$$

Then, we can derive a discrete-time state-space model of the general form as

$$\dot{x}_{k+1} = f(x_k, u_k) + v_k := f_0(x_k) + \sum_{i=1}^{3} g(x_k)u_k + v_k. \tag{30}$$

Note that this model can be linear if we consider linearized viscous and tether forces, i.e.

$$f(x_k, u_k) = A_0 x_k + B_0 u_k \ ,$$

where the matrix A_0 is given by

$$A_0 = \begin{pmatrix} \mathbf{0}_{6\times6} & I_6 & \mathbf{0}_{6\times36} \\ -M_{inv}(K_p + K_H) & -M_{inv}B_v & -M_{inv}C_r \\ \mathbf{0}_{36,\times6} & B_r & A_r \end{pmatrix},$$

with $M_{inv} = (M_{tot} + A_{inf})^{-1}$, and the matrix B_0 is given by

$$B_0 = \begin{pmatrix} \mathbf{0}_{6\times6} \\ M_{inv}B_u \\ \mathbf{0}_{36\times6} \end{pmatrix}.$$

Here and in the following, we use I_n to denote an identity matrix of dimension $n \times n$.

A controllability analysis on the linearized system was reported in [18] for a very similar WEC device, via the computation of a frequency-based relative gain array (RGA), which shows that (at the nominal position of the buoy $\mathbf{X} = \mathbf{0}_{6\times1}$) the pitch θ_x and roll θ_y motions are less controllable than the surge x_g, sway y_G and heave z_G motions. We will see in the numerical results section that the estimates of wave force over pitch and roll motions are less accurate. The poor controllability over these motion directions may be one reason.

For simplicity, we suppose that the covariance matrix Q_k takes the form of

$$Q_k = \begin{pmatrix} \mathbf{0} & \mathbf{0} \\ \mathbf{0} & Q_{k,22} \end{pmatrix}, \tag{31}$$

with $Q_{k,22} \in \mathbf{R}^{n_z \times n_z}$ being a positive definite diagonal matrix.

The observations of the system are supposed to be the generalized position $\mathbf{X}$ and speed $\dot{\mathbf{X}}$ of the buoy. Therefore, the observation model is simply

$$z_k = Cx_k + w_k, \tag{32}$$

where w_k are measurement noises. The matrix C takes the form

$$C = \begin{pmatrix} I_{n_z} & \mathbf{0}_{n_z \times (n_x - n_z)} \end{pmatrix}. \tag{33}$$

Now that we have the process model (30) and the observation model (32), we can apply the SCKF. Unfortunately, direct application of the SCKF fails because of the convergence problems due to the huge differences in the magnitudes of state components : while f_e is of order 1×10^6-1×10^7, the other components are of order 1 or less. We propose in the next section a remedy to this problem: introducing a state scaling factor to bring all components back to similar magnitudes.

C. State scaling

Instead of using directly f_e in the state (29), we replace it with a scaled state x_e which satisfies

$$x_e = s_e f_e,$$

where $s_e \in \mathbf{R}^6 = (s_{e,1}, \cdots, s_{e,6})$ with $s_{e,i} > 0$ small enough. Obviously, by choosing a suitable scaling factor s_e, we can get similar magnitudes for all components of the state.

In the following, we show an additional advantage of introducing this scaling factor. Considering the process model (30), due to the random walk model (28), we have

$$A_k = \nabla f(\hat{x}_{k|k}, u_k) = \begin{pmatrix} A_{k,11} & \mathbf{0} \\ \mathbf{0} & I_{n_e} \end{pmatrix}$$

with $n_e = 6$ the dimension of the wave excitation force, and $v_k = (\mathbf{0}_{(n_x - n_z) \times 1}, v_e(k))$. Let us decompose matrix $P_{k+1|k}$ as

$$P_{k+1|k} = \begin{pmatrix} P_{11} & P_{12} \\ P_{21} & P_{22} \end{pmatrix},$$

where $P_{11} \in \mathbf{R}^{n_z \times n_z}$ and the other matrices are of suitable dimensions. Taking into account the form of matrix C (33), the transition matrix (18) becomes

$$\begin{aligned} \Phi(k+1,k) &= \left(I - P_{k+1|k} C^T P^{-1}_{zz,k+1|k} C \right) \beta_k A_k \\ &= \begin{pmatrix} * & * & \mathbf{0} \\ * & * & \mathbf{0} \\ \mathbf{0} & \mathbf{0} & I_{n_e} \end{pmatrix}, \end{aligned} \tag{34}$$

with $*$ some non-zero matrices. The identity I_{n_e} at the right bottom of the transition matrix $\Phi(k+1,k)$ confirms our intuition: the random walk model (28) produces bounded wave force estimates but preserves as well the estimation error.

Keeping this in mind, we can see that the scaling factor s_e indirectly reduces the process noise. Indeed, rewriting (28) with the scaled state, we have

$$x_e(k+1) = x_e(k) + s_e v_e(k), \tag{35}$$

and hence the state noise v_k in the process model (30) becomes $v_k = (\mathbf{0}_{(n_x - n_z) \times 1}, s_e v_e(k))$, which is much smaller.

Remark 2: By setting an appropriate state scaling factor s_e, the undesirable large estimation errors on the yaw direction (reported in [7]) can be avoided.

In the next section, we propose a heuristic method to adjust the matrix Q_k, which is later shown to be efficient by numerical experiments.

D. Choice of Q_k

In order to avoid divergence or performance degradation of standard SCKF due to the inadequate prior knowledge on model noise statistics, the matrices Q_k and R_k should be chosen to ensure stability of the algorithm while trying to decrease estimation errors.

Since the covariance matching techniques are among the most popular methods to achieve this, we give here a brief recall. The covariance matrix of the measurement noise can be estimated from (see e.g. [19])

$$\hat{R}_k = \mathbf{E}[\Delta z_k \Delta_k^T] - C P_{k|k-1} C^T, \tag{36}$$

where $\Delta \bar{z} = \frac{1}{N} \sum_{j=1}^{N} \Delta z_{k-j}$ and

$$\mathbf{E}[\Delta z_k \Delta_k^T] = \frac{1}{N-1} \sum_{j=1}^{N} (\Delta z_{k-j} - \Delta \bar{z})(\Delta z_{k-j} - \Delta \bar{z})^T$$

can be estimated with a limited number of innovation samples with an estimation window N. A similar estimation exists also for the covariance matrix Q_k if the system is completely observable

$$C \hat{Q}_k C^T = E[\Delta z_k \Delta_k^T] + E[r_k r_k^T] - C(P_{k|k} + P_{k|k-1}) C^T, \tag{37}$$

where $r_k = z_k - C x_{k|k}$.

Unfortunately, these commonly used covariance estimation approaches are not applicable in our case. Indeed, we observe from numerical experiments that (36) gives rise to negative definite R_k, and (37) gives no information about how we should adjust the Q_k defined by (31). Keeping in mind that the choice of Q_k and R_k can be other than the real covariance matrices, we propose to design our Q_k with a heuristic method.

As mentioned in Section II, it is in general sufficient to adjust only one of the matrices R_k and Q_k, so we will fix the matrix R_k in this paper. As for Q_k, inspired by (23), we adjust it according to the following heuristic method:

1) Perform a numerical sensitivity analysis by modifying each non-zero component of Q_k and observing its influence on the innovation $\Delta z_{k+1|k}$.
2) Adjust Q_k according to the sensitivity analysis results, in a component-wise manner.

In this heuristic method, the normalized mean square error goodness-of-fit (GoF) is used to quantify the sensitivity analysis results. The GoF is given by the expression

$$GoF = 1 - NMSE = 1 - \frac{\|s(t) - \tilde{s}(t)\|_2}{\|s(t) - \bar{s}(t)\|_2}, \tag{38}$$

where $s(t)$ is the time domain reference signal (the "true" wave excitation force f_e, fed to the plant model), the bar notation denotes the mean value, $\tilde{s}(t)$ is the estimated signal, and the notation $\| \cdot \|_2$ represents the L2-norm of a vector [20]. GoF = 1 (or 100%, when expressed in percentage) would denote perfect estimation of the reference wave excitation force component.

Let us present an example. According to the sensitivity analysis, increasing the third diagonal component of $Q_{k,22}(3,3)$ leads to an increase of the the GoF of the

9th component of the innovation. Then, we can adjust the corresponding component of $Q_{k,22}$ by

$$Q_{k,22}(3,3) = c_{q,3,3} \cdot GoF^k_{innov}(9), \tag{39}$$

where $c_{q,3,3}$ a tuning hyper-parameter, and GoF^k_{innov} denotes the GoF of the innovation computed at step k. The matrix Q_k is adaptively adjusted during the estimation: every N_q estimator steps, we compute GoF^k_{innov} using the last N_q gathered innovations, and then update the corresponding components of the Q_k matrix. Here we use a window of size N_q to alleviate the computational burden associated to GoF^k_{innov}.

Note that the hyper-parameters should be carefully chosen, as too large values may yield accurate estimates under ideal conditions (without measurement noises), and yet lead to significant inaccuracies in the presence of measurement noises. We will see a numerical example in the next section.

To sum up, for our SCKF estimator, according to the sensitivity analysis, we need to choose only 3 hyper-parameters: one for the third, the fourth, and the fifth diagonal component of $Q_{k,22}$, respectively. We tune and fix these hyper-parameters based on simulations performed on a single sea state in the presence of observation noises. For all the other test sea states, we use the same hyper-parameters and let the algorithm adjust the matrix Q_k every N_q estimator steps. Numerical results will show the efficiency of this procedure.

IV. NUMERICAL RESULTS

A. Implementation and numerical setting

Recall that the dimension of the state x is $n_x = 72$ (6 for $\mathbf{X}$, 6 for $\dot{X}$, and 54 for $\mathbf{X}_r$) and the dimension of the observation z is $n_z = 12$ (6 for $\mathbf{X}$, 6 for $\dot{X}$). The dimensions being quite high, the real-time implementation of the SCKF with the nonlinear process model becomes less straightforward. Fortunately, steps (3), (4), (7), (8) in the SCKF can be parallelized. The parallelization of the evaluation on the $2n_x$ cubature points, especially on the propagated cubature points (4), makes the algorithm much more efficient.

In addition, we distinguish the SCKF time step from the system simulation time step: we apply the time update and measurement update of the SCKF every $N_{step} \geq 1$ of the system simulation time. In general, this comes at a price: the greater N_{step}, the less accurate the estimator. Therefore, N_{step} should be chosen large enough, while still ensuring acceptable performance.

In our experiments, the measurements $\mathbf{X}$ and $\dot{\mathbf{X}}$ are obtained by simulating the full model (24), with an artificially generated wave signal and a spring-damper feedback control law

$$u_i = -k_{l,i} l_i - k_{ldot,i} \dot{l}_i, \quad i = 1, \cdots, 3,$$

where coefficients $k_{l,i}$ and $k_{ldot,i}$ are tuned by grid search to maximize the mean energy production. Measurement noises with normal distributions are then added to simulated data. More precisely, we add to each measurement component a noise $w_i \sim \mathcal{N}(\mu\sigma_i, 1)$, where $\mu > 0$ is the chosen noise level and σ_i is the variance of the i-th component data.

In the following, we will simulate the WEC behavior under the action of realistic short-crested irregular waves, obtained using a $cos - 2s$ directional spreading function around the main wave direction θ_0

$$D(\theta) = cos\left(\frac{1}{2}(\theta - \theta_0)\right)^{2s}. \tag{40}$$

Moreover, for all numerical tests presented hereafter, we set $N_{step} = 5$ and the state scaling factor $s_e = (1 \times 10^6, \cdots, 1 \times 10^6, 1)$.

B. A case study

In this section, we present in details results of a case study. A first comparison will show that our heuristic method to adapt the matrix Q_k dramatically improves the quality of wave excitation force estimation, and a second comparison will give a hint on the tuning of the heuristic parameters.

We consider the case with noise level $\mu = 0.1$ and an irregular wave signal having characteristics $T_p = 14\,\mathrm{s}$ (peak wave period), $H_s = 3\,\mathrm{m}$ (significant wave height), $\theta_0 = 60°$ (mean direction) and $s = 5$ (spreading coefficient).

In Table I, the GoF of the observations $\mathbf{X}$ and $\dot{\mathbf{X}}$ are given for the test with both constant and adaptive matrices Q_k. We can see that the heuristic proposed in section III-D significantly improves the GoF of the 4-th component of $\mathbf{X}$ and the 4-th and the 5-th components of $\dot{\mathbf{X}}$. These improvements lead to a significant accuracy increase of f_e estimates over the roll and the pitch motions, as shown in Fig. 2 and Fig. 3.

Constant Q_k and R_k						
GoF of $\mathbf{X}$	99.96	99.97	99.97	96.62	98.98	99.21
GoF of $\dot{\mathbf{X}}$	99.73	99.75	98.33	63.37	85.73	99.34
GoF of f_e	85.39	84.52	93.78	-38.16	-35.06	-
Adaptive Q_k and R_k						
GoF of $\mathbf{X}$	99.96	99.97	99.97	99.98	99.97	99.07
GoF of $\dot{\mathbf{X}}$	99.73	99.74	99.53	99.61	99.73	99.19
GoF of f_e	90.28	90.76	92.95	89.70	87.94	-

TABLE I
GOF (IN %) OF THE MEASUREMENTS AND THE WAVE MOMENT ESTIMATES. NOISE LEVEL $\mu = 0.1$.

In Table II, the GoF of the f_e estimates without noise ($\mu = 0$) and with noise level $\mu = 0.05$ are given. We can see that the measurement noises degrade a bit the estimation accuracy, which however remains acceptable.

	Suege	Sway	Heave	Roll	Pitch
$\mu = 0$	97.06	96.50	98.52	92.67	91.36
$\mu = 0.05$	95.41	95.10	97.97	91.86	91.41

TABLE II
GOF (IN %) OF WAVE MOMENT ESTIMATES.

Now we deal with the same wave signal, but set all components of Q_k to be 10 times larger than those of the previous test. In Table III, the GoF of the wave force estimates are given for different noise levels. Compared to Table II, we can see that, when there is no measurement noise ($\mu = 0$), the GoF of the wave estimates with larger Q_k is higher. However, the larger Q_k leads to serious degradation in the cases with measurement

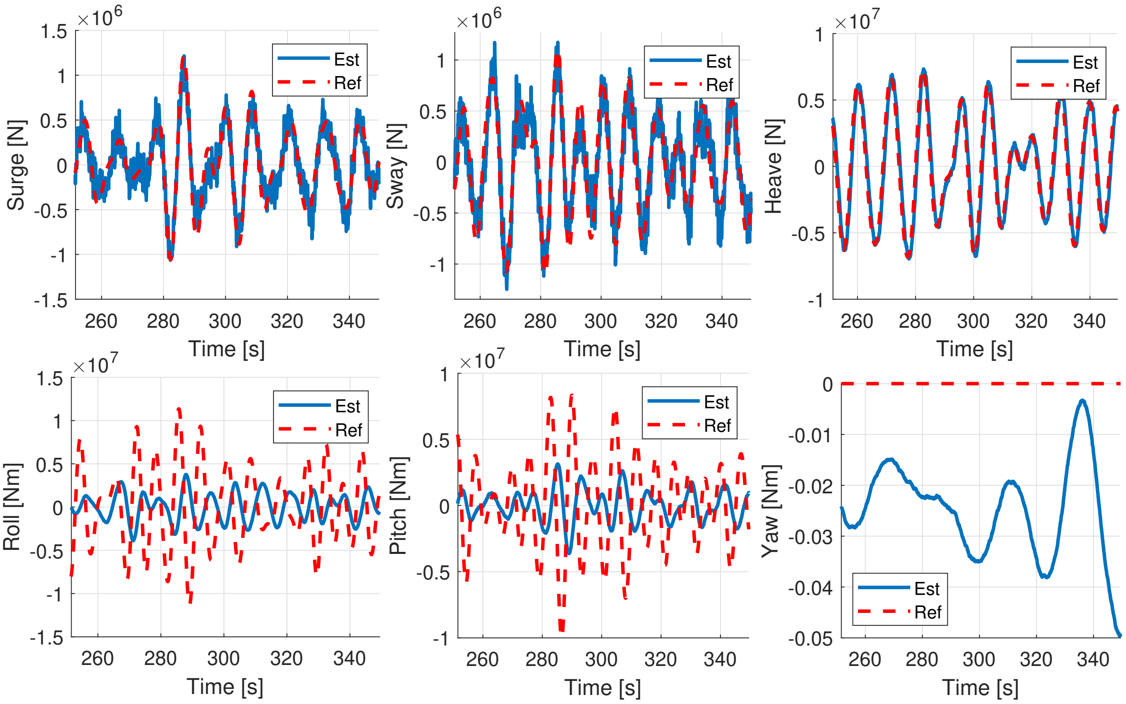

Fig. 2. Comparison of f_e and its estimate. Wave signal characteristics: $T_p = 12\,\mathrm{s}, H_s = 3\,\mathrm{m}, \theta_0 = 60°, s = 5$. Noise level $\mu = 0.1$.

noises, especially over heave, roll, and pitch motions. An intuitive explication for this phenomenon is that when the measurement is quite noisy, one needs to place less reliance on the measurement and instead place greater trust in the process model (by setting Q_k smaller).

	Suege	Sway	Heave	Roll	Pitch
$\mu = 0$	97.37	96.76	99.17	99.72	99.35
$\mu = 0.05$	95.52	95.27	64.13	-127.41	-407.23
$\mu = 0.1$	89.91	90.64	-42.88	-893.61	-2245.11

TABLE III
GOF (IN %) OF WAVE MOMENT ESTIMATES : OBTAINED WITH LARGER VALUES OF Q_k COMPONENTS.

In the next section, we apply the SCKF with the tuned heuristic method to a set of irregular wave signals, and show that the proposed method give acceptable estimation results for all the tested signals.

C. Additional results

To evaluate the estimator performance, in addition to the GoF, we consider also the mean lag (or delay) between the real signal and the estimated one. The mean lag is estimated via cross-correlation, using the Matlab function `finddelay`. The mean lag should not be larger than the sampling time that will be used for control.

A set of short-crested irregular wave signals are generated (all with a spreading coefficient $s = 5$). Those sea states represent a wide variety of scenarios, both in terms of the main wave direction, which excites predominantly different modes of motion, and in terms of wave steepness, which enhance the non-linear dynamics.

Estimation results with different noise levels under these irregular wave signals are summarized in Table IV-VI. We can see that the wave estimator works well: results show higher GoF in surge, sway, and heave axes, with a small degradation in roll and pitch axes. The GoF decreases with larger measurement noises, but remains acceptable.

As for the mean lag, any value not larger than the sampling time of the control system using the wave excitation force estimates, should be considered acceptable. Following the lines of [7], 0.5 s should be a reasonable value for the 25 m-diameter buoy considered in this work. In our experiments, the system integration time step was set to 0.01 s and the SCKF updates time step was 0.05 s (with $N_{step} = 5$). We can see from Table IV-VI that the estimator gives good enough mean lags.

Remark 3: Several parameters of our heuristic method need to be tuned, such as the parameter $c_{q,3,3}$ in (39). However, it is worth noting that the tuning procedure has proven to be quite simple: we have conducted the sensitivity analysis and tuned the parameters with the case study of section IV-B with noise level $\mu = 0.1$. The resulting parameters turned out to be good enough to obtain acceptable estimator performance for all the tests of this section.

V. CONCLUSION

In a multi-DoF context, this paper has introduced a readily adjustable SCKF framework for estimating the wave excitation force acting on a submerged WEC. The estimator has been designed based on a nonlinear state-space system of order 66 of a CETO 6 - like device, and tested with a set of multi-directional (short-crested)

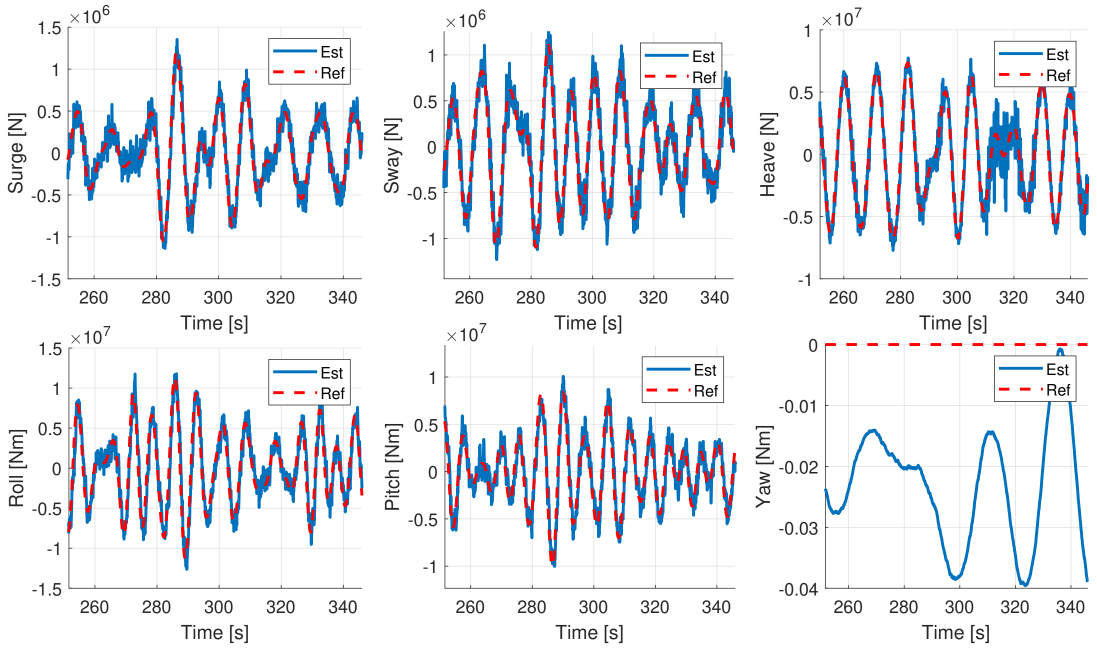

Fig. 3. Comparison of f_e and its estimate: with Q_k and R_k adjustments. Wave signal characteristics: $T_p = 12\,\mathrm{s}, H_s = 3\,\mathrm{m}, \theta_0 = 60°, s = 5$. Noise level $\mu = 0.1$.

irregular wave signals. With a careful state scaling and a heuristic method to adapt the process noise covariance matrix Q_k, we have obtained consistently good estimation results in all motion directions, despite the presence of measurement (observation) noises.

REFERENCES

[1] B. A. Ling, "Real-time estimation and prediction of wave excitation forces for wave energy control applications," 2015.

[2] A. J. Hillis, C. Whitlam, A. Brask, J. Chapman, and A. R. Plummer, "Power capture gains for the wavesub submerged wec using active control," in *Proceedings of the Thirteenth European Wave and Tidal Energy Conference. EWTEC, Naples, Italy*, 2019.

[3] A. Hillis, J. Yardley, A. Plummer, and A. Brask, "Model predictive control of a multi-degree-of-freedom wave energy converter with model mismatch and prediction errors," *Ocean Engineering*, vol. 212, p. 107724, 2020.

[4] H.-N. Nguyen and P. Tona, "Wave excitation force estimation for wave energy converters of the point-absorber type," *IEEE Transactions on Control Systems Technology*, vol. 26, no. 6, pp. 2173–2181, 2017.

[5] E. A. Wan and R. Van Der Merwe, "The unscented kalman filter for nonlinear estimation," in *Proceedings of the IEEE 2000 Adaptive Systems for Signal Processing, Communications, and Control Symposium (Cat. No. 00EX373)*. Ieee, 2000, pp. 153–158.

[6] I. Arasaratnam and S. Haykin, "Cubature kalman filters," *IEEE Transactions on automatic control*, vol. 54, no. 6, pp. 1254–1269, 2009.

[7] H.-N. Nguyen, P. Tona, A. Mérigaud, M. Cocho, and A. Pichard, "Wave excitation force estimation for a multi-dof wec via a cubature kalman filter: Design and preliminary results," in *International Conference on Offshore Mechanics and Arctic Engineering*, vol. 85192. American Society of Mechanical Engineers, 2021, p. V009T09A016.

[8] I. Arasaratnam, S. Haykin, and T. R. Hurd, "Cubature kalman filtering for continuous-discrete systems: theory and simulations," *IEEE Transactions on Signal Processing*, vol. 58, no. 10, pp. 4977–4993, 2010.

[9] K. Xiong, L. Liu, and H. Zhang, "Modified unscented kalman filtering and its application in autonomous satellite navigation," *Aerospace Science and Technology*, vol. 13, no. 4-5, pp. 238–246, 2009.

[10] R. P. Agarwal, *Difference equations and inequalities: theory, methods, and applications*. CRC Press, 2000.

[11] S. Sastry, *Nonlinear systems: analysis, stability, and control*. Springer Science & Business Media, 2013, vol. 10.

[12] B. Zhou and T. Zhao, "On asymptotic stability of discrete-time linear time-varying systems," *IEEE Transactions on Automatic Control*, vol. 62, no. 8, pp. 4274–4281, 2017.

[13] J. Zarei, E. Shokri, and H. R. Karimi, "Convergence analysis of cubature kalman filter," in *2014 European Control Conference (ECC)*. IEEE, 2014, pp. 1367–1372.

[14] M. Boutayeb and D. Aubry, "A strong tracking extended kalman observer for nonlinear discrete-time systems," *IEEE Transactions on Automatic Control*, vol. 44, no. 8, pp. 1550–1556, 1999.

[15] S. C. Rutan, "Adaptive kalman filtering," *Analytical Chemistry*, vol. 63, no. 22, pp. 1103A–1109A, 1991.

[16] M. Folley, *Numerical modelling of wave energy converters: state-of-the-art techniques for single devices and arrays*. Academic Press, 2016.

[17] J. Scruggs, S. Lattanzio, A. Taflanidis, and I. Cassidy, "Optimal causal control of a wave energy converter in a random sea," *Applied Ocean Research*, vol. 42, pp. 1–15, 2013.

[18] N. Sergiienko, B. Cazzolato, M. Arjomandi, B. Ding, and L. da Silva, "Considerations on the control design for a three-tether wave energy converter," *Ocean Engineering*, vol. 183, pp. 469–477, 2019.

[19] Y. Meng, S. Gao, Y. Zhong, G. Hu, and A. Subic, "Covariance matching based adaptive unscented kalman filter for direct filtering in ins/gnss integration," *Acta Astronautica*, vol. 120, pp. 171–181, 2016.

[20] A. F. Davis and B. C. Fabien, "Wave excitation force estimation of wave energy floats using extended kalman filters," *Ocean Engineering*, vol. 198, p. 106970, 2020.

	Surge		**Sway**		**Heave**		**Roll**		**Pitch**	
	GoF	Lag	GoF	Lag	GoF	Lag	GoF	Lag	GoF	Lag
$T_p = 8\,\mathrm{s}, H_s = 1\,\mathrm{m}, \theta_0 = 0^\circ$	95.84	0.25	96.00	0.20	98.11	0.15	90.39	0.30	90.48	0.30
$T_p = 8\,\mathrm{s}, H_s = 1\,\mathrm{m}, \theta_0 = 30^\circ$	94.85	0.25	95.24	0.25	98.05	0.15	91.16	0.30	90.94	0.30
$T_p = 8\,\mathrm{s}, H_s = 1\,\mathrm{m}, \theta_0 = 60^\circ$	95.25	0.25	94.82	0.25	98.21	0.15	91.34	0.30	90.50	0.30
$T_p = 10\,\mathrm{s}, H_s = 2\,\mathrm{m}, \theta_0 = 0^\circ$	95.88	0.25	96.10	0.25	98.56	0.15	93.58	0.25	91.55	0.30
$T_p = 10\,\mathrm{s}, H_s = 2\,\mathrm{m}, \theta_0 = 30^\circ$	95.90	0.25	95.98	0.25	98.64	0.15	93.05	0.30	91.61	0.30
$T_p = 10\,\mathrm{s}, H_s = 2\,\mathrm{m}, \theta_0 = 60^\circ$	96.01	0.25	95.76	0.25	98.68	0.15	92.84	0.30	91.88	0.30
$T_p = 12\,\mathrm{s}, H_s = 2\,\mathrm{m}, \theta_0 = 0^\circ$	96.68	0.25	97.22	0.25	98.44	0.15	95.96	0.20	91.71	0.30
$T_p = 12\,\mathrm{s}, H_s = 2\,\mathrm{m}, \theta_0 = 30^\circ$	96.83	0.25	96.79	0.25	98.08	0.20	93.59	0.25	91.25	0.30
$T_p = 12\,\mathrm{s}, H_s = 2\,\mathrm{m}, \theta_0 = 60^\circ$	97.06	0.25	96.50	0.25	98.52	0.15	92.67	0.30	91.36	0.30
$T_p = 14\,\mathrm{s}, H_s = 3\,\mathrm{m}, \theta_0 = 0^\circ$	97.18	0.25	96.06	0.25	98.73	0.15	87.08	0.25	92.49	0.25
$T_p = 14\,\mathrm{s}, H_s = 3\,\mathrm{m}, \theta_0 = 30^\circ$	97.14	0.25	95.93	0.25	98.67	0.15	89.23	0.30	90.97	0.30
$T_p = 14\,\mathrm{s}, H_s = 3\,\mathrm{m}, \theta_0 = 60^\circ$	96.92	0.25	96.68	0.25	98.60	0.15	91.80	0.30	88.59	0.30

TABLE IV

Noise level $\mu = 0$: NMSE-GoF (in %) and mean lags (in s) of wave moment estimates

.

	Surge		**Sway**		**Heave**		**Roll**		**Pitch**	
	GoF	Lag	GoF	Lag	GoF	Lag	GoF	Lag	GoF	Lag
$T_p = 8\,\mathrm{s}, H_s = 1\,\mathrm{m}, \theta_0 = 0^\circ$	94.10	0.25	95.00	0.20	98.00	0.15	90.31	0.30	90.42	0.30
$T_p = 8\,\mathrm{s}, H_s = 1\,\mathrm{m}, \theta_0 = 30^\circ$	94.12	0.25	94.38	0.25	97.93	0.15	91.00	0.30	90.56	0.30
$T_p = 8\,\mathrm{s}, H_s = 1\,\mathrm{m}, \theta_0 = 60^\circ$	94.27	0.25	94.01	0.25	98.04	0.15	91.15	0.30	90.67	0.30
$T_p = 10\,\mathrm{s}, H_s = 2\,\mathrm{m}, \theta_0 = 0^\circ$	95.50	0.25	95.70	0.25	98.39	0.15	93.31	0.25	91.41	0.30
$T_p = 10\,\mathrm{s}, H_s = 2\,\mathrm{m}, \theta_0 = 30^\circ$	95.51	0.25	95.56	0.25	98.62	0.15	92.79	0.30	91.57	0.30
$T_p = 10\,\mathrm{s}, H_s = 2\,\mathrm{m}, \theta_0 = 60^\circ$	95.62	0.25	95.40	0.25	98.61	0.15	92.76	0.30	91.91	0.30
$T_p = 12\,\mathrm{s}, H_s = 2\,\mathrm{m}, \theta_0 = 0^\circ$	95.54	0.25	95.81	0.25	98.02	0.15	93.36	0.20	91.65	0.30
$T_p = 12\,\mathrm{s}, H_s = 2\,\mathrm{m}, \theta_0 = 30^\circ$	95.21	0.25	95.78	0.25	97.68	0.15	92.50	0.25	90.74	0.30
$T_p = 12\,\mathrm{s}, H_s = 2\,\mathrm{m}, \theta_0 = 60^\circ$	95.41	0.25	95.10	0.25	97.97	0.15	91.85	0.30	91.41	0.30
$T_p = 14\,\mathrm{s}, H_s = 3\,\mathrm{m}, \theta_0 = 0^\circ$	95.81	0.25	94.00	0.25	98.44	0.15	84.48	0.25	91.95	0.25
$T_p = 14\,\mathrm{s}, H_s = 3\,\mathrm{m}, \theta_0 = 30^\circ$	95.97	0.25	94.47	0.25	98.47	0.15	88.11	0.30	90.68	0.30
$T_p = 14\,\mathrm{s}, H_s = 3\,\mathrm{m}, \theta_0 = 60^\circ$	95.93	0.25	95.42	0.25	98.15	0.15	90.59	0.30	89.32	0.30

TABLE V

Noise level $\mu = 0.05$: NMSE-GoF (in %) and mean lags (in s) of wave moment estimates

.

	Surge		**Sway**		**Heave**		**Roll**		**Pitch**	
	GoF	Lag	GoF	Lag	GoF	Lag	GoF	Lag	GoF	Lag
$T_p = 8\,\mathrm{s}, H_s = 1\,\mathrm{m}, \theta_0 = 0^\circ$	91.92	0.25	92.16	0.20	95.91	0.15	89.83	0.30	90.00	0.30
$T_p = 8\,\mathrm{s}, H_s = 1\,\mathrm{m}, \theta_0 = 30^\circ$	92.06	0.25	91.82	0.25	96.60	0.15	90.37	0.30	89.98	0.30
$T_p = 8\,\mathrm{s}, H_s = 1\,\mathrm{m}, \theta_0 = 60^\circ$	91.65	0.25	91.81	0.25	96.41	0.15	90.87	0.30	90.30	0.30
$T_p = 10\,\mathrm{s}, H_s = 2\,\mathrm{m}, \theta_0 = 0^\circ$	94.48	0.25	94.73	0.25	96.89	0.15	92.76	0.25	91.09	0.30
$T_p = 10\,\mathrm{s}, H_s = 2\,\mathrm{m}, \theta_0 = 30^\circ$	94.25	0.25	94.40	0.25	97.85	0.10	92.29	0.25	91.29	0.30
$T_p = 10\,\mathrm{s}, H_s = 2\,\mathrm{m}, \theta_0 = 60^\circ$	94.38	0.25	94.31	0.25	97.38	0.10	92.32	0.30	91.84	0.30
$T_p = 12\,\mathrm{s}, H_s = 2\,\mathrm{m}, \theta_0 = 0^\circ$	92.10	0.25	91.39	0.25	93.52	0.10	84.87	0.20	90.39	0.30
$T_p = 12\,\mathrm{s}, H_s = 2\,\mathrm{m}, \theta_0 = 30^\circ$	90.72	0.25	92.54	0.25	92.22	0.15	88.95	0.25	89.16	0.30
$T_p = 12\,\mathrm{s}, H_s = 2\,\mathrm{m}, \theta_0 = 60^\circ$	90.28	0.25	90.76	0.25	92.95	0.15	89.70	0.30	87.94	0.25
$T_p = 14\,\mathrm{s}, H_s = 3\,\mathrm{m}, \theta_0 = 0^\circ$	91.78	0.25	88.18	0.25	95.45	0.10	79.24	0.25	87.94	0.25
$T_p = 14\,\mathrm{s}, H_s = 3\,\mathrm{m}, \theta_0 = 30^\circ$	92.52	0.25	89.73	0.25	95.57	0.10	83.48	0.30	86.98	0.25
$T_p = 14\,\mathrm{s}, H_s = 3\,\mathrm{m}, \theta_0 = 60^\circ$	93.06	0.25	91.56	0.25	94.40	0.10	85.80	0.30	86.07	0.25

TABLE VI

Noise level $\mu = 0.1$: NMSE-GoF (in %) and mean lags (in s) of wave moment estimates

.